Letter Vol. 50, No. 2 / 15 January 2025 / Optics Letters 257

Optics Letters

Boundary-artifact-free quantitative phase imaging with Fourier ptychographic microscopy

Yao Jin,[1,2,3,†] Yefeng Shu,[1,2,3,†] Yuzhen Zhang,[1,2,3,4] Jiasong Sun,[1,2,3,*] and Chao Zuo[1,2,3,5]

[1]Smart Computational Imaging Laboratory (SCILab), School of Electronic and Optical Engineering, Nanjing University of Science and Technology, Nanjing, Jiangsu Province 210094, China
[2]Smart Computational Imaging Research Institute (SCIRI) of Nanjing University of Science and Technology, Nanjing, Jiangsu Province 210019, China
[3]Jiangsu Key Laboratory of Spectral Imaging & Intelligent Sense, Nanjing, Jiangsu Province 210094, China
[4]zyz_1973@njust.edu.cn
[5]zuochao@njust.edu.cn
[†]These authors contributed equally to this work.
[*]sunjiasong@njust.edu.cn

Received 25 September 2024; revised 26 October 2024; accepted 26 November 2024; posted 26 November 2024; published 2 January 2025

Fourier ptychographic microscopy (FPM) enables high-resolution, wide-field imaging of both amplitude and phase, presenting significant potential for applications in digital pathology and cell biology. However, artifacts commonly observed at the boundaries of reconstructed images can significantly degrade imaging quality and phase retrieval accuracy. These boundary artifacts are typically attributed to the use of the fast Fourier transform (FFT) on non-periodic images. Another significant physical factor that should not be overlooked is the transverse diffraction of light across boundaries. Here, we introduce a boundary extension reconstruction framework for FPM, termed BE-FPM, which provides boundary-artifact-free quantitative phase imaging (QPI) with minimal computational overhead. In this method, the reconstructed image is initialized with zero-padding and then self-extrapolated during the subsequent iterative reconstruction process. This approach allows for partial restoration of the sample beyond the boundary, ensuring sample consistency around the boundary and addressing the boundary artifact problem fundamentally. We demonstrate the effectiveness of the proposed BE-FPM on both microlens array and live cells, establishing it as an effective FPM solver for boundary-artifact-free QPI and accurate phase characterization for various types of samples.

https://doi.org/10.1364/OL.542725

Fourier ptychographic microscopy (FPM) [1,2] is a well-established high-throughput imaging tool for achieving high-resolution and large field of view (FOV) simultaneously. The technology efficiently enables quantitative phase imaging (QPI) with non-interferometric synthetic aperture through angular illumination scanning and computational reconstruction. Since its invention in 2013, FPM achieves remarkable advances in imaging throughput improvement in both space [3,4] and time [5,6], efficient phase retrieval algorithm [7,8], system error self-calibration [9,10], tomography [11,12], and low-cost and easy-to-implement realization [13,14]. The significant improvements in imaging capacity and robustness make FPM a promising tool for parallel analysis of a large population of cells across a wide FOV, which is invaluable for fields of drug development, medical diagnostics, and personalized genomics [15,16].

For the purpose of correcting the spatially varying imaging aberrations [9] and improving computational efficiency, the captured raw images of FPM are generally divided into multiple subregions for independent and parallel reconstruction. The problem of boundary artifact prevents successful stitching of subregions and hinders FPM from obtaining a seamless full-FOV reconstruction. More importantly, the boundary problem will cause misestimation of the recovered phase height, which could limit the use of FPM in certain applications, such as potentially affecting the accuracy of cell dry mass measurements. A well-known cause of the boundary problem is the implementation of the fast Fourier transform (FFT) on an aperiodic image, which brings the ripple-shaped artifact [17]. A similar problem in QPI based on the transport of intensity (TIE) is solved by introducing a rectangular aperture diaphragm to directly obtain the boundary values [18]. Correspondingly, the discrete cosine transform [18] or iterative phase retrieval algorithm [19] is applied to solve the boundary conditions. However, these works address the problem by incurring additional hardware and computation resource consumption. Hence, an embedded scheme with high computational efficiency for solving boundary problems is expected to be developed. In digital image processing, a method called periodic plus smooth image decomposition [20] aims to solve the boundary problem by separating the image into the object and the artifact in the Fourier domain, and it is further extended to FPM [21]. However, it is risky to remove artifacts in the algorithm solely through digital image processing based on prior assumptions but without a solid physical model.

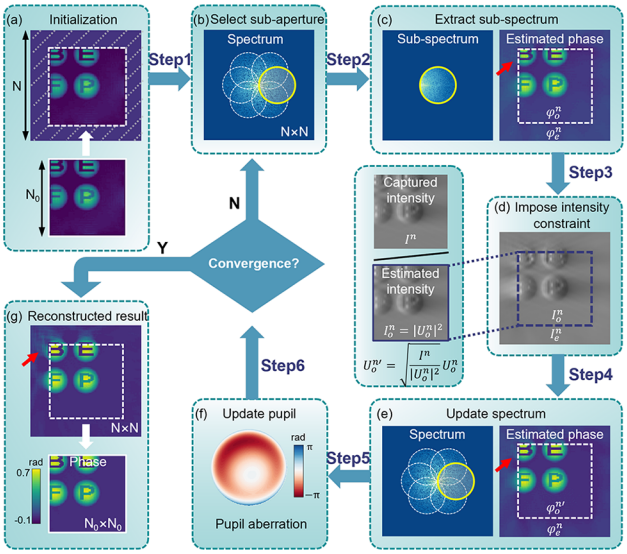

Fig. 1. Flow chart of the BE-FPM model.

Another physical factor that has not been seriously examined previously is the transverse diffraction of stray light from the sample beyond the FOV boundary into the reconstruction field. In traditional FPM iterative procedures, the sample is cut off around the boundary where its consistency cannot be assured, leading to stray light being mistakenly reconstructed in the phase map and resulting in artifacts. We refer to this phenomenon as transverse diffraction artifact, which will be further elucidated in the following sections. We observe that the experimentally captured FOV can be extrapolated through iterative processes, allowing for the retrieval of samples beyond the established boundary [22]. This approach ensures the consistency of the sample, thereby inspiring us to address the boundary problem in FPM by drawing on this innovative idea.

In this Letter, we report an efficient FPM reconstruction framework to solve the boundary problem, called boundary extension FPM (BE-FPM). In this method, the reconstructed image is extended with zero pixels in initialization and extrapolated in subsequent iterative reconstructions. The sample beyond the experimentally captured FOV is retrieved to ensure consistency around the boundary, thus eliminating transverse diffraction artifacts. In addition, the extrapolation of the FOV prevents the reconstruction of the ripple artifact caused by the FFT on the boundary of the captured FOV. After the convergence of iterations, the captured FOV is segmented from the extrapolated FOV as the final reconstructed result, effectively eliminating both artifacts. The proposed method requires no additional hardware, effectively solves the boundary problem in FPM with little increase in computation and iteration rounds, and guarantees accurate phase retrieval, which has been validated on both standard and biological samples.

BE-FPM can be viewed as an extension of our previous framework of adaptive optical QPI (AO-QPI) [23], which additionally solves the boundary problem in FPM phase retrieval. Figure 1 illustrates the reconstruction procedures of BE-FPM, where a simulated microlens array is adopted as a demonstration sample. Six intensity images captured under NA-matched illuminations are adopted as the raw dataset for reconstruction, efficiently enabling an accurate characterization of sample and pupil function. In the first step [Fig. 1(a)], the raw intensity images (with an image size of $N_0 \times N_0$ pixels) are used to initialize a complex amplitude image, which is then placed in the center of the extended FOV (with an enlarged image size of $N \times N$ pixels, where N is αN_0 and α is set between 1.1 and 1.2). The initialized phase map is obtained by intensity deconvolution using the calculated phase transfer function [6]. The phase values of the extended area are set to zero. The captured images are then used successively to update the corresponding apertures on the initialized spectrum in each iteration. For the updating process of nth aperture, a sub-spectrum is obtained through filtering the spectrum using pupil function and is then Fourier transformed to generate an estimated complex amplitude U^n, as shown in Figs. 1(b) and 1(c). Here, the estimated complex amplitude can be divided into two parts spatially:

$$U^n = U_o^n + U_e^n. \tag{1}$$

U_o^n and U_e^n separately denote the complex amplitudes in the center region and the extended FOV where the central value is zero. Then, the intensity constraint of the captured image I^n is imposed on U_o^n as follows:

$$U_o^{n\prime} = \sqrt{\frac{I^n}{|U_o^n|^2}}\, U_o^n, \tag{2}$$

where $U_o^{n\prime}$ is the updated complex amplitude of the central FOV, as shown in Fig. 1(d). And the full updated complex amplitude $U^{n\prime}$ is calculated as follows:

$$U^{n\prime} = U_o^{n\prime} + U_e^n. \tag{3}$$

The obtained $U^{n\prime}$ is Fourier transformed and then updated into the n aperture of the reconstructed spectrum following a typical FPM updating formula [1] [Fig. 1(e)]. Simultaneously, the calculated $U_o^{n\prime}$ is also used to update the pupil function following the updating formula stated in [23], as shown in Fig. 1(f). Considering the boundary artifacts in U_o^n are properly removed in iterations, a more accurate characterization of the system pupil function is expected to be achieved here. The updating process for each aperture of the spectrum is repeated until the iterative optimization converges. For the reconstructed result, as shown in Fig. 1(g), we can see that the part of the sample beyond the boundary is reconstructed in the extended FOV (see red arrow); hence, the sample consistency around the boundary is properly satisfied and the artifacts are effectively eliminated.

To validate the effectiveness of BE-FPM in addressing boundary problems, we performed the simulation under three representative boundary conditions and compared the results with the traditional algorithm [1]. The sample (a microlens array) and illumination mode (six LEDs under matched illumination configuration; see Fig. 2(a)) for simulation are consistent with Fig. 1. Figures 2(b1)–2(b3) show raw intensity images of three different regions cropped from the full FOV, which are identified by colored boxes in Fig. 2(a). The phase maps reconstructed by the traditional algorithm are provided in Figs. 2(c1)–2(c3), as well as the corresponding maps of the phase error. The ripple artifacts can be observed at the boundaries of the three images, which are caused by the aperiodicity of the raw intensity images (see white arrows). The transverse diffraction artifact is evident in the first phase map (see red arrow). More importantly, the phase of the sample is underestimated when the sample spans across the boundary, which can be seen from the comparison between Figs. 2(c1) and 2(c3).

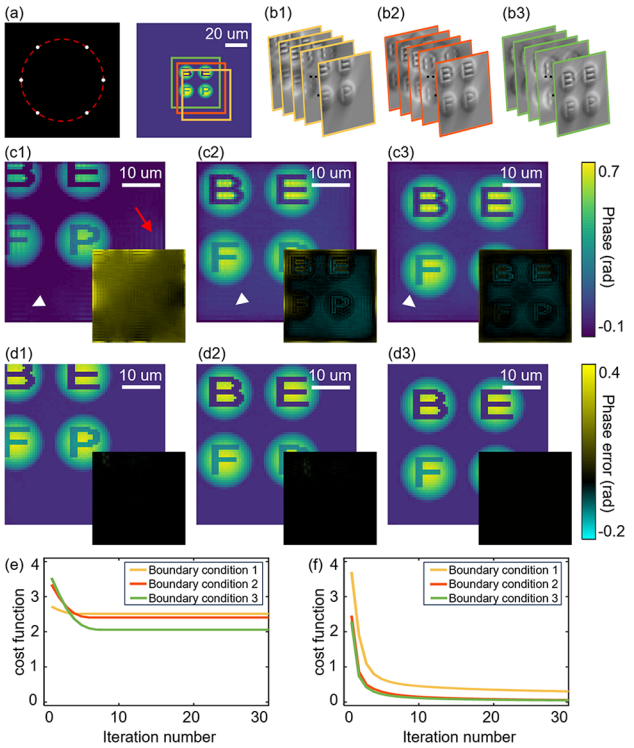

Fig. 2. Simulation results of the microlens array under different boundary conditions using the traditional FPM and BE-FPM. (a) Illumination mode (left) and ground truth of phase (right). (b1)–(b3) Raw intensity images corresponding to different boundary conditions. (c1)–(c3) Phase reconstruction and error maps obtained using the traditional FPM. (d1)–(d3) Phase reconstruction and error maps obtained using BE-FPM. (e) Convergence curves of the reconstruction using the traditional FPM under different boundary conditions. (f) Convergence curves of the reconstruction using BE-FPM under different boundary conditions.

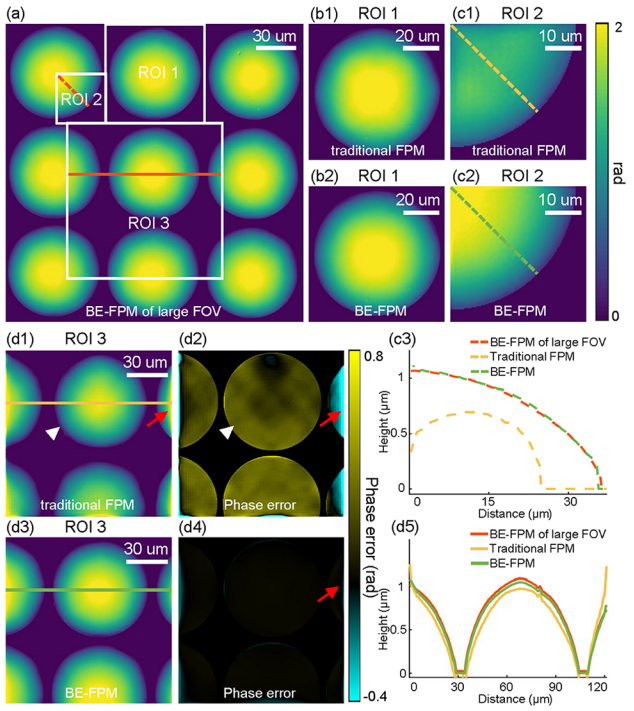

Fig. 3. Experimental results on a standard microlens array sample. (a) Reconstructed full-FOV phase of the microlenses. (b1), (b2) Reconstructed phase of ROI 1 using the traditional FPM and BE-FPM, respectively. (c1), (c2) Reconstructed phase of ROI 2 using the traditional FPM and BE-FPM, respectively. (c3) Thickness profiles taken along the dashed lines in 3(a), 3(c1), and 3(c2). (d1)–(d4) Reconstructed phase and error maps of ROI 3 using the traditional FPM and BE-FPM, respectively. (d5) Thickness profiles taken along the red, yellow, and green lines in 3(a), 3(d1), and 3(d3).

The convergence lines for the three conditions in Fig. 2(e) indicate that the traditional algorithm cannot guarantee a universal solution for any boundary condition. The convergence is worst when the sample crosses the boundary, which is consistent with the error maps shown in Figs. 2(c1)–2(c3). As a comparison, Figs. 2(d1)–2(d3) and 2(f) provide the reconstructed phase maps and convergence curves using the proposed BE-FPM. The ripple artifacts at the boundaries are eliminated and the phase reconstruction accuracy is promised for the three boundary conditions. The corresponding iterative cost functions under the three conditions achieve fast convergence.

To further experimentally demonstrate the phase retrieval accuracy improvement after solving the boundary problem, we perform BE-FPM on a microlens array (SUSS, MicroOptics), where each unit has a diameter of 75 μm, a curvature radius of 0.5 mm, and a height of 1.4 μm. The experiment was performed by using an inverted microscope (IX71, Olympus, Japan) equipped with a 4×, 0.16 NA objective and a programmable annular LED with an illumination wavelength of 550 nm. Following the simulation configuration, six intensity images captured under matched illumination were adopted as the raw dataset. A support constraint was imposed on the phase map in reconstruction for a more correct solution, where a mask was applied to set the background phase value of the microlens array to zero. Figure 3(a) displays the phase reconstruction of a large FOV containing a 3×3 microlens array. Three representative boundary condition cases are demonstrated here by selecting subregions of ROI 1, ROI 2, and ROI 3 for reconstruction. Figures 3(b1) and 3(b2) show the phase results of ROI 1. Since the microlens unit is located in the center of the image and does not cross the boundary, there is no significant difference between the results of the traditional algorithm and BE-FPM. In the other case, ROI 2 contains a quarter of a microlens unit, which exceeds the upper and left boundaries. As can be seen in Fig. 3(c3), the microlens height recovered by the traditional algorithm is significantly lower compared to the theoretical value. As for the third case, a more complex condition is demonstrated in ROI 3, where multiple microlenses are completely or partially located in the FOV. We provide the recovered phase maps of both algorithms [Figs. 3(d1) and 3(d3)], as well as the corresponding phase error maps [Figs. 3(d2) and 3(d4)] and phase profiles [Fig. 3(d5)]. It can be seen that although the microlens is completely in the FOV, the reconstruction accuracy can still be significantly affected (see white arrow) if the boundary condition is not properly handled during the reconstruction process. More serious errors occur at the boundary (see red arrow), where the phase value exceeds the theoretical value by ~1 rad. Application of the BE-FPM solves these problems and promises an accurate reconstruction for each unit in the FOV. Generally, the provided experimental results on the microlens array have validated that our method successfully solves the boundary problem in FPM, avoiding

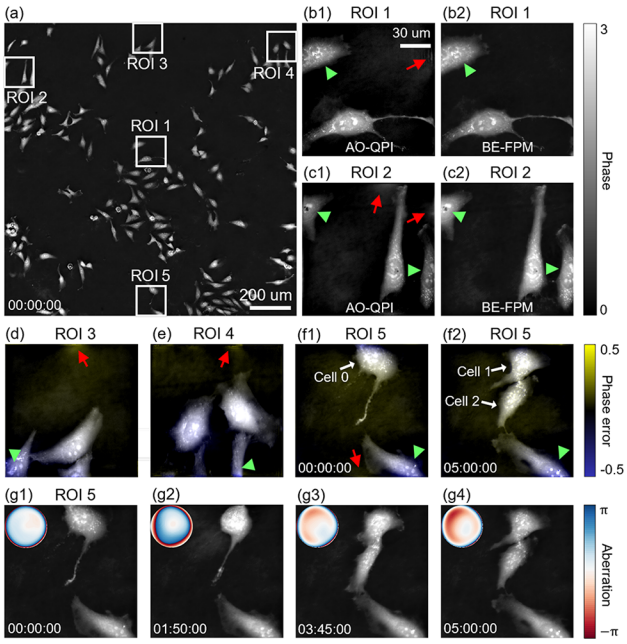

Fig. 4. Dynamic imaging of HeLa live cells (Visualization 1). (a) One frame of the phase reconstruction with a full FOV of 1.77 mm^2. (b1), (b2) Reconstructed phase of ROI 1 using AO-QPI and BE-FPM, respectively. (c1), (c2) Reconstructed phase of ROI 2 using AO-QPI and BE-FPM, respectively. (d), (e) Phase reconstruction using BE-FPM and error maps of ROI 3 and ROI 4. (f1), (f2) Phase reconstruction using BE-FPM and error maps of the first and last frames in ROI 5. (g1)–(g4) Dynamic tracking images of cells in ROI 5.

the boundary artifacts and achieving a more accurate phase characterization.

In Fig. 4, we performed BE-FPM for dynamic imaging on unstained human breast cancer cells (HeLa cells) over 5 h with a wide FOV of 1.77 mm^2 [see Visualization 1]. HeLa cells were cultured in a 37°C incubator with 5% carbon dioxide, and 16-bit raw images were captured with a 10×, 0.4 NA objective and a CMOS camera of 6.5 μm pixel size. The full FOV was divided into 100 subregions for parallel reconstruction, and cell dynamics, such as migration and reproduction, inevitably led to changes in boundary conditions of each subregion. Figure 4(a) shows the first frame of the full FOV. Boundary artifact removal in each subregion is significant for the reconstruction of the full FOV, indicating that no overlapping areas are needed between the 100 subregions, allowing for the direct splicing of Fig. 4(a) with no visible joints. We compare the reconstruction results of ROI 1 and ROI 2 using AO-QPI [Figs. 4(b1)–4(c1)] and BE-FPM [Figs. 4(b2)–4(c2)]. The red arrows indicate the ripple and transverse diffraction artifacts in the AO-QPI, and the green triangles highlight the differences in phase height between the results of the two algorithms. The trend of cell phase reduction due to boundary conditions is consistent with the standard microlens sample [Fig. 3(d1)], demonstrating that BE-FPM can measure phase in live cell imaging. Figures 4(d)–4(f2) further demonstrate the phase reconstruction results of BE-FPM and the difference between BE-FPM and AO-QPI with color emphasized phase error. Over 5 h, Cell 0 in ROI 5 finally divided into two daughter cells, with red arrows depicting the change of boundary conditions as the cell moved away from the boundary. To further validate the applicability of BE-FPM under real-time varying boundary conditions, we selected four different frames of ROI 5 to display the phase results and corresponding aberrations, as shown in Figs. 4(g1)–4(g4). Experimental results reveal the capability of BE-FPM to address boundary conditions arising from time-varying aberrations and cellular dynamics.

Generally, the proposed BE-FPM effectively solves the boundary problem with very little increase in computational consumption. Two kinds of boundary artifacts occur in the traditional algorithm: the ripple artifacts caused by the aperiodicity of the image and the transverse diffraction artifacts when the sample crosses the FOV. These are eliminated here, promising high-quality phase imaging, especially for a large stitched FOV. We have validated the proposed method in theoretical simulation and experiments on standard phase target samples. It has been demonstrated that BE-FPM can perform accurate phase retrieval under boundary conditions, which cannot be achieved by the traditional algorithm. The experimental results indicate that we provide a powerful ptychographic solver to achieve boundary-artifact-free phase retrieval for live cell research in the biomedical field. It should be noted that BE-FPM may face challenges in reconstructing large phase targets in high-speed shooting situations. In the future, we will focus on this problem and it is expected to promote the BE-FPM algorithm to tomographic phase microscopy. It is foreseeable that the boundary problem also affects accurate refractive index reconstruction in a 3D volume, which deserves a more in-depth exploration.

Funding. National Key Research and Development Program of China (2022YFA1205002, 2024YFE0101300); National Natural Science Foundation of China (62105151, 62175109, U21B2033, 62227818, 62361136588); Leading Technology of Jiangsu Basic Research Plan (BK20192003); Biomedical Competition Foundation of Jiangsu Province (BE2022847); Key National Industrial Technology Cooperation Foundation of Jiangsu Province (BZ2022039).

Disclosures. The authors declare no conflicts of interest.

Data availability. Data underlying the results presented in this paper are not publicly available but may be obtained from the authors upon reasonable request.

REFERENCES

1. G. Zheng, R. Horstmeyer, and C. Yang, Nat. Photonics **7**, 739 (2013).
2. S. Jiang, P. Song, T. Wang, *et al.*, Nat. Protoc. **18**, 2051 (2023).
3. J. Sun, C. Zuo, L. Zhang, *et al.*, Sci. Rep. **7**, 1187 (2017).
4. A. Pan, Y. Zhang, K. Wen, *et al.*, Opt. Express **26**, 23119 (2018).
5. L. Tian, Z. Liu, L.-H. Yeh, *et al.*, Optica **2**, 904 (2015).
6. J. Sun, C. Zuo, J. Zhang, *et al.*, Sci. Rep. **8**, 7669 (2018).
7. L. Bian, J. Suo, G. Zheng, *et al.*, Opt. Express **23**, 4856 (2015).
8. T. Nguyen, Y. Xue, Y. Li, *et al.*, Opt. Express **26**, 26470 (2018).
9. X. Ou, G. Zheng, and C. Yang, Opt. Express **22**, 4960 (2014).
10. R. Eckert, Z. F. Phillips, and L. Waller, Appl. Opt. **57**, 5434 (2018).
11. C. Zuo, J. Sun, J. Li, *et al.*, Opt. Lasers Eng. **128**, 106003 (2020).
12. S. Xu, X. Yang, P. Ritter, *et al.*, Adv. Photonics **6**, 026004 (2024).
13. T. Aidukas, R. Eckert, A. R. Harvey, *et al.*, Sci. Rep. **9**, 7457 (2019).
14. K. C. Lee, K. Lee, J. Jung, *et al.*, ACS Photonics **8**, 1307 (2021).
15. A. C. Chan, J. Kim, A. Pan, *et al.*, Sci. Rep. **9**, 11114 (2019).
16. O. Akcakir, L. K. Celebi, M. Kamil, *et al.*, Biomed. Opt. Express **13**, 3904 (2022).
17. V. Volkov, Y. Zhu, and M. De Graef, Micron **33**, 411 (2002).
18. C. Zuo, Q. Chen, and A. Asundi, Opt. Express **22**, 9220 (2014).
19. L. Huang, C. Zuo, M. Idir, *et al.*, Opt. Lett. **40**, 1976 (2015).
20. L. Moisan, J. Math Imaging Vis. **39**, 161 (2011).
21. A. Pan, A. Wang, J. Zheng, *et al.*, Opt. Lasers Eng. **162**, 107408 (2023).
22. T. Latychevskaia and H.-W. Fink, Opt. Express **21**, 7726 (2013).
23. Y. Shu, J. Sun, J. Lyu, *et al.*, PhotoniX **3**, 24 (2022).